

Modeling three-dimensional underwater acoustic propagation over multi-layered fluid seabeds using the equivalent source method

Tengjiao He,^{1,a)} Shiqi Mo,^{1,a),b)} Erzheng Fang,^{1,a)} Mingguang Wang,^{1,a)} and Rui Zhang²

¹Acoustic Science and Technology Laboratory, Harbin Engineering University, Harbin 150001, China

²Jiangsu Automation Research Institute, Lianyungang 222061, China

ABSTRACT:

This paper develops an efficient three-dimensional (3D) underwater acoustic propagation model with multi-layered fluid seabeds based on the equivalent source method (ESM). It solves the Helmholtz equation exactly by a superposition of fields generated by equivalent sources. A linear system coupling ESM equations is derived by imposing boundary conditions and solved iteratively using the generalized minimum residual method. Unlike a direct ESM solver, matrix–vector products in each iteration are evaluated by a pre-corrected fast Fourier transformation (PFFT), significantly reducing the numerical cost and enabling efficient solution of 3D large-scale propagation. Moreover, sound speed profiles can be taken into account by dividing the water column into sub-layers, each of which requires an individual PFFT procedure using an FFT subgrid scheme. Simulations of propagation over a Gaussian canyon validate the PFFT-accelerated ESM (PFFT-ESM). The capability of the PFFT-ESM for 3D scattering problems is demonstrated by further presenting the Gaussian canyon simulations with corrugated surface waves.

© 2021 Acoustical Society of America. <https://doi.org/10.1121/10.0006663>

(Received 8 June 2021; revised 11 September 2021; accepted 22 September 2021; published online 18 October 2021)

[Editor: Nicholas P. Chotiros]

Pages: 2854–2864

I. INTRODUCTION

Three-dimensional (3D) full-wave simulations, obtained by numerical models based on the Helmholtz equation, are essential for benchmarking underwater acoustic propagation with complex topographies. They are also useful for investigating 3D propagation effects, such as horizontal refraction and transverse coupling. Generally, the approximation of the wave equation is required to implement 3D underwater acoustic propagation models on modern PC platforms, for example, the paraxial approximation in the parabolic equation (PE) and the eikonal equation for the ray tracing. The PE method offers a one-way wave equation solution, thus predicting accurate results in underwater environments with negligible back-scattering. In addition, the phase errors induced by the PE approximation restrict angles around the dominant propagation direction (Jensen *et al.*, 2011). On the other hand, the ray tracing is a high-frequency approximation and needs corrections to caustics and shadow zones. Finding eigenrays becomes more complicated for complex topographies in 3D scenarios (Jensen *et al.*, 2011). Besides, it fails to capture the horizontal diffraction accurately where the bottom derivative is discontinuous (Porter, 2019). Further numerical efforts are required to improve the applicabilities of the approximations (Sturm,

2016; Lingeitch *et al.*, 2002; Collins and Evans, 1992), increasing the computational burdens on either the PE or the ray tracing to obtain 3D full-wave simulations.

With the rapid development of computational power, several numerical models have been developed to solve the Helmholtz equation exactly, including the finite element method (FEM), spectral element method (SEM), boundary element method (BEM), and equivalent source method (ESM). Recently, there has been growing interest in using the FEM to model underwater propagation (Isakson *et al.*, 2014), scattering (Isakson *et al.*, 2014), and reverberation (Isakson and Chotiros, 2011). The FEM solves the weak form of the Helmholtz equation by discretizing the physical domain. With careful treatments of meshing, the FEM can provide benchmark-quality solutions without any approximations. Another attractive aspect of the FEM is the versatility for geometries and material properties treated in simulations. Since the FEM is fully customized, it is very suitable for benchmarking 2D problems with complex environment parameters. Nevertheless, computational power restricts the meshing size, thus the problem size. To extend the FEM to 3D underwater propagation, a longitudinal invariant finite element (LIFE) model has been proposed by Isakson *et al.* (2014). However, geometry and environment parameters treated in this model are restricted to be translationally symmetric. Also, involving volume discretization, the SEM has been widely used to model underwater propagation in the time domain (Cristini and Komatitsch, 2012; Bottero *et al.*, 2016; Bottero *et al.*, 2018). The SEM utilizes

^{a)}Also at: Key Laboratory of Marine Information Acquisition and Security (Harbin Engineering University), Ministry of Industry and Information Technology, Harbin 150001, China.

^{b)}Electronic mail: moshiqi@hrbeu.edu.cn

a high-order piecewise polynomial approximation to the weak formulation of the Helmholtz equation, enabling a numerically efficient full-wave solution of the wavefield. Although the SEM has been extended to handle 3D underwater propagation at low frequencies (Xie *et al.*, 2016), the problem size may be restricted since the SEM still relies on volume discretization.

Apart from the above methods, boundary integral equation (BIE)-based methods have increasingly been applied to underwater acoustic propagation. The BIE-based method solves the Helmholtz boundary-value problem exactly but significantly reduces computational load by discretizing the boundary, rather than the whole physical domain. Siderius and Porter (2008) utilized a Helmholtz–Kirchhoff approximation (HKA) integral to model broadband sound transmissions in the ocean with time-varying sea surfaces. Although this model can be extended to 3D scenarios straightforwardly, additional efforts are required to correct the high-frequency approximation, and the seabed is assumed to be flat. Several literature pieces have demonstrated BEM’s capability for both 2D propagation and 3D propagation with translational symmetry (Godinho *et al.*, 2001; Pereira *et al.*, 2010). In the BEM-based propagation model, a linear system coupling all boundary integrals needs to be solved, involving a dense $N \times N$ coefficient matrix (N is the number of unknown pressures and normal pressure gradients on the boundary). Generally, the linear system can be solved using either the Gaussian elimination at a numerical cost of $O(N^3)$ or the iterative method at $O(N^2)$. When dealing with 3D large-scale propagation, the BEM requires a huge amount of operations and an impractical memory to generate and store the dense matrix, respectively. A recent study proposed a direct 3D numerical sound propagation model by combining the BEM with the pre-corrected fast Fourier transform (PFFT) technique (Li *et al.*, 2019). A key aspect of the PFFT technique involved is that it significantly reduces the numerical cost of evaluating matrix–vector products (Phillips and White, 1997), and so the memory savings achieved in this model make it suitable for the numerical solution of large-scale underwater acoustic propagation on modern PC platforms. The PFFT technique is particularly suitable for incorporating integral-based methods when dealing with boundary-value problems.

As an alternative to the BEM, the ESM was developed to handle the field radiated by a complex radiator initially and has been applied to underwater acoustic propagation recently (Abawi and Porter, 2007; He *et al.*, 2020; He *et al.*, 2021). The ESM has two advantages over the BEM (Koopmann *et al.*, 1989): (1) numerical implementation is simpler since the basis functions are nodes rather than elements; (2) the BEM’s inherent singularity is circumvented by retracing the equivalent sources from their corresponding boundaries. Similarly, a dense matrix is involved in the ESM, transferring equivalent sources to their corresponding boundaries. A direct ESM solver, therefore, is impractical for 3D large-scale propagation. To the best of our knowledge, no ESM-based propagation model with accelerated algorithms has been extended to 3D large-scale propagation

yet. This paper aims to bridge this gap by combining a 3D ESM-based propagation model with the PFFT technique.

This paper first derives the equivalent source equation governing the sound field in a waveguide overlaying a multi-layered fluid seabed, with the surface-reflected, seabed-reflected, and seabed-transmitted fields replaced with the fields generated by a few sets of equivalent sources. By imposing boundary conditions at the sea surface and the interfaces between two fluid layers, a linear system is derived, and this is then solved iteratively using the generalized minimum residual method (GMRM). The GMRM is employed because: (a) it is a Krylov subspace method to solve linear systems with asymmetric matrices $[A]$, converging rapidly with an appropriate preconditioner; (b) it enables the matrix-free iteration, which is suitable for incorporating with the PFFT. In each iteration step, the matrix–vector product is evaluated using the PFFT technique. This technique projects strengths of equivalent sources onto a uniform fast Fourier transform (FFT) grid, converting a matrix–vector multiplication to a 3D convolution. In this way, the numerical cost is reduced from $O(N^{2-3})$ for a direct ESM solver to $O(N_g \log N_g)$ (where N and N_g are the numbers of equivalent sources and FFT grid points). A scheme of FFT subgrids is proposed to improve the computational efficiency for multi-layered scenarios further. The PFFT-accelerated ESM (PFFT-ESM) is validated by comparison with the LIFE model in the scenario of propagation over a Gaussian canyon, and its capability for 3D scattering from sea surfaces is demonstrated by presenting the Gaussian canyon simulations with corrugated surface waves.

The primary contributions of this paper are: (a) accelerated by the iterative GMRM solver and the fast evaluation of the matrix–vector product, the ESM is extended to 3D large-scale computations. The PFFT-ESM enables a full-wave simulation of 3D large-scale underwater propagation to be performed on a standard computer rather than supercomputers to which most of the researchers cannot get easy access; (b). Numerical schemes are proposed to improve the computational efficiency of the PFFT-ESM further, including the selection of a preconditioner according to the stand-off distance of equivalent sources and an optimized scheme of FFT subgrids for a stratified water column. The remainder of the paper is organized as follows: Sec. II presents the formulae of the 3D ESM and the PFFT, Sec. III presents numerical simulations, and conclusions are drawn in Sec. IV.

II. THREE-DIMENSIONAL UNDERWATER ACOUSTIC PROPAGATION MODEL USING THE PRE-CORRECTED FAST FOURIER TRANSFORM-ACCELERATED EQUIVALENT SOURCE METHOD

A. An equivalent source method-based propagation model with multi-layered fluid seabeds

As shown in Fig. 1, consider the range-dependent shallow water with a sound speed and density of c_w and ρ_w ,

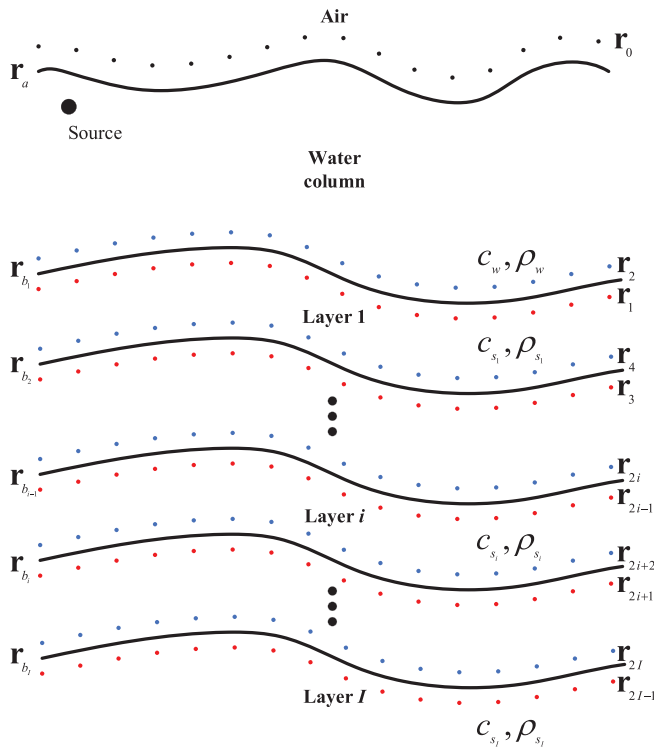


FIG. 1. (Color online) Scheme of ESM for shallow water overlying a multi-layered fluid seabed, with black, blue, and red solid circles denoting those equivalent sources replacing the surface-reflected field, the seabed-reflected field and the seabed-transmitted field, respectively.

overlying a fluid seabed of I layers. The sound speed and the density of the i th layer of the seabed are c_{s_i} and ρ_{s_i} ($i = 1, 2, \dots, I$), respectively. Here, the subscripts w and s specify the water and seabed layers, respectively. The positions of the surface and the interface between the i th layer and its upper layer are \mathbf{r}_a and \mathbf{r}_{b_i} , respectively. The Helmholtz equation governing the sound field $p(\mathbf{r})$ in the waveguide is given by

$$[\nabla^2 + k^2]p(\mathbf{r}) = 0, \tag{1}$$

where $\mathbf{r} = (x, y, z)$ is the position vector, and k is the wave-number that becomes $k_w = \omega/c_w$ in water and $k_s = \omega/c_s$ in the seabed, where ω is the angular frequency. The pressure-release boundary condition at \mathbf{r}_a and the continuity of pressure and displacement at \mathbf{r}_{b_i} can be expressed as

$$\begin{cases} p(\mathbf{r}_a) = 0, \\ p(\mathbf{r}_{b_i})_- = p(\mathbf{r}_{b_i})_+, \\ u(\mathbf{r}_{b_i})_- = u(\mathbf{r}_{b_i})_+, \end{cases} \tag{2}$$

where u is the normal displacement at \mathbf{r}_{b_i} . The equivalent source method (ESM) will express the solution of Eq. (1) by a superposition of basis functions (the Green's functions), with the unknown coefficients of the basis functions solved by imposing the boundary conditions defined in Eq. (2). The Green's functions have the mathematical expressions of $G^{sp}(\mathbf{r}; \mathbf{r}'|k) = 1/4\pi(e^{jk|\mathbf{r}-\mathbf{r}'|}/|\mathbf{r}-\mathbf{r}'|)$ for sound pressure and of $G^u(\mathbf{r}; \mathbf{r}'|k) = \frac{1}{\rho\omega^2} \hat{\mathbf{n}} \nabla G^{sp}(\mathbf{r}; \mathbf{r}'|k)$ for normal displacement, automatically satisfying the Sommerfeld radiation condition. Here, \mathbf{r}' is the position of the point source, $\hat{\mathbf{n}}$ represents the unit normal vector to the corresponding boundary, and k and ρ are the wavenumber and the density that will subsequently change according to the position of the receiver.

Based on the ESM, the waveguide field can be separated into the incident field, the surface-reflected field, the seabed-reflected field, and the seabed-transmitted field. In the water column, the sound field is separated into the incident field and the fields reflected by the boundaries at \mathbf{r}_a and \mathbf{r}_{b_1} . In the i th seabed layer ($i < I$), the sound field is the summation of the field transmitted in the layer and the field reflected by the lower boundary of the layer, while only the seabed-transmitted field exists in the I th layer. Accordingly, one set of equivalent sources is placed above the sea surface at \mathbf{r}_0 , replacing the surface-reflected field. For each interface between two fluid layers at \mathbf{r}_{b_i} , two sets of equivalent sources are utilized, placed above the interface at $\mathbf{r}_{(2i)}$ and below the interface at $\mathbf{r}_{(2i-1)}$, which replaces the seabed-transmitted field in the i th layer and the seabed-reflected field in the upper layer, respectively. The solution of Eq. (1) then can be written as (Abawi and Porter, 2007)

$$\begin{cases} p_w(\mathbf{r}) = p_{inc}(\mathbf{r}) + \sum_{n=1}^N G^{sp}(\mathbf{r}; \mathbf{r}_{(0)}|k_w)s_{(0)n} + \sum_{n=1}^N G^{sp}(\mathbf{r}; \mathbf{r}_{(1)}|k_w)s_{(1)n}, & \mathbf{r} \in \text{water} \\ p_s(\mathbf{r}) = \sum_{n=1}^N G^{sp}(\mathbf{r}; \mathbf{r}_{(2i)}|k_{s_i})s_{(2i)n} + \sum_{n=1}^N G^{sp}(\mathbf{r}; \mathbf{r}_{(2i+1)}|k_{s_i})s_{(2i+1)n}, & \mathbf{r} \in \text{sediment } (i < I) \\ p_s(\mathbf{r}) = \sum_{n=1}^N G^{sp}(\mathbf{r}; \mathbf{r}_{(2I)}|k_{s_I})s_{(2I)n}, & \mathbf{r} \in \text{basement } (i = I) \end{cases} \tag{3}$$

where p_{inc} is the incident field, N is the number of each set of equivalent sources, and $s_{(0,1,2i,2i+1)n}$ is the unknown source strength for the n th source. The solution for displacement in the waveguide has the similar expression as Eq. (3), superposed by

the displacement Green's functions. By imposing the boundary conditions defined in Eq. (2) at N nodes at each boundary, a linear system is derived, coupling all fields generated by $2I + 1$ sets of equivalent sources (He et al., 2021):

$$\begin{cases}
 \mathbf{G}^{SP}(\mathbf{r}_a; \mathbf{r}_{(0)}|k_w)\mathbf{s}_{(0)} + \mathbf{G}^{SP}(\mathbf{r}_a; \mathbf{r}_{(1)}|k_w)\mathbf{s}_{(1)} = -\mathbf{p}_{inc}(\mathbf{r}_a), \\
 \mathbf{G}^{SP}(\mathbf{r}_{b_1}; \mathbf{r}_{(0)}|k_w)\mathbf{s}_{(0)} + \mathbf{G}^{SP}(\mathbf{r}_{b_1}; \mathbf{r}_{(1)}|k_w)\mathbf{s}_{(1)} - \mathbf{G}^{SP}(\mathbf{r}_{b_1}; \mathbf{r}_{(2)}|k_{s_1})\mathbf{s}_{(2)} - \mathbf{G}^{SP}(\mathbf{r}_{b_1}; \mathbf{r}_{(3)}|k_{s_1})\mathbf{s}_{(3)} = -\mathbf{p}_{inc}(\mathbf{r}_{b_1}), \\
 \mathbf{G}^U(\mathbf{r}_{b_1}; \mathbf{r}_{(0)}|k_w)\mathbf{s}_{(0)} + \mathbf{G}^U(\mathbf{r}_{b_1}; \mathbf{r}_{(1)}|k_w)\mathbf{s}_{(1)} - \mathbf{G}^U(\mathbf{r}_{b_1}; \mathbf{r}_{(2)}|k_{s_1})\mathbf{s}_{(2)} - \mathbf{G}^U(\mathbf{r}_{b_1}; \mathbf{r}_{(3)}|k_{s_1})\mathbf{s}_{(3)} = -\mathbf{u}_{inc}(\mathbf{r}_{b_1}). \\
 \vdots \\
 \mathbf{G}^{SP}(\mathbf{r}_{b_i}; \mathbf{r}_{(2i-2)}|k_{s_{i-1}})\mathbf{s}_{(2i-2)} + \mathbf{G}^{SP}(\mathbf{r}_{b_i}; \mathbf{r}_{(2i-1)}|k_{s_{i-1}})\mathbf{s}_{(2i-1)} - \mathbf{G}^{SP}(\mathbf{r}_{b_i}; \mathbf{r}_{(2i)}|k_{s_i})\mathbf{s}_{(2i)} \\
 - \mathbf{G}^{SP}(\mathbf{r}_{b_i}; \mathbf{r}_{(2i+1)}|k_{s_i})\mathbf{s}_{(2i+1)} = 0, \\
 \mathbf{G}^U(\mathbf{r}_{b_i}; \mathbf{r}_{(2i-2)}|k_{s_{i-1}})\mathbf{s}_{(2i-2)} + \mathbf{G}^U(\mathbf{r}_{b_i}; \mathbf{r}_{(2i-1)}|k_{s_{i-1}})\mathbf{s}_{(2i-1)} - \mathbf{G}^U(\mathbf{r}_{b_i}; \mathbf{r}_{(2i)}|k_{s_i})\mathbf{s}_{(2i)} \\
 - \mathbf{G}^U(\mathbf{r}_{b_i}; \mathbf{r}_{(2i+1)}|k_{s_i})\mathbf{s}_{(2i+1)} = 0 \\
 \vdots \\
 \mathbf{G}^{SP}(\mathbf{r}_{b_l}; \mathbf{r}_{(2l-2)}|k_{s_{l-1}})\mathbf{s}_{(2l-2)} + \mathbf{G}^{SP}(\mathbf{r}_{b_l}; \mathbf{r}_{(2l-1)}|k_{s_{l-1}})\mathbf{s}_{(2l-1)} - \mathbf{G}^{SP}(\mathbf{r}_{b_l}; \mathbf{r}_{(2l)}|k_{s_l})\mathbf{s}_{(2l)} = 0, \\
 \mathbf{G}^U(\mathbf{r}_{b_l}; \mathbf{r}_{(2l-2)}|k_{s_{l-1}})\mathbf{s}_{(2l-2)} + \mathbf{G}^U(\mathbf{r}_{b_l}; \mathbf{r}_{(2l-1)}|k_{s_{l-1}})\mathbf{s}_{(2l-1)} - \mathbf{G}^U(\mathbf{r}_{b_l}; \mathbf{r}_{(2l)}|k_{s_l})\mathbf{s}_{(2l)} = 0,
 \end{cases} \tag{4}$$

where \mathbf{p}_{inc} and \mathbf{u}_{inc} are the $N \times 1$ incident pressure and normal displacement vectors at the corresponding boundaries, $\mathbf{G}^{u,SP}$ represents the transfer matrix with its entries being $G^{u,SP}(\mathbf{r}_m; \mathbf{r}_{(2i-2, 2i-1, 2i, 2i+1)}|k)$, and $\mathbf{s}_{(2i-2, 2i-1, 2i, 2i+1)}$ is the $N \times 1$ strength vector of equivalent sources located at $\mathbf{r}_{(2i-2, 2i-1, 2i, 2i+1)}$. Here, \mathbf{r}_m is the position of the m th receiver. The above linear system can be expressed as $[A]\{x\} = \{b\}$ which can be solved using either the Gaussian elimination at a numerical cost of $O(N^3)$ or the iterative method at a numerical cost of $O(N^2)$. A straightforward linear system solution is numerically expensive for large-scale propagation, requiring an impractical amount of random access memory (RAM) to store the dense matrix $[A]$. In this paper, the linear system is solved using the generalized minimum residual method (GMRM). For the GMRM, the matrix–vector product $[A]\{x\}$ in each iteration is evaluated using the pre-corrected fast Fourier transform (PFFT) technique without an explicit expression of $[A]$. Consequently, the numerical cost is reduced from $O(N^{2-3})$ to $O(N_g \log N_g)$, where N_g is the number of the FFT grids. The PFFT will be detailed in the next section. After solving the linear system, the waveguide field can be calculated using Eq. (3).

B. Pre-corrected fast Fourier transform technique

In the PFFT technique, a 3D block is first defined to contain all the equivalent sources and their corresponding boundaries and is then subdivided into several small cubes, each of which contains a few equivalent sources, as shown in Fig. 2(a). The cubes are referred to as cells. The basic idea of the PFFT is to evaluate the distant source–receiver interaction using a few weighted Green’s functions for point sources on a uniform grid throughout the cell volume (a locally weighted grid-to-grid interaction), while the near-field source–receiver interaction between neighboring cells is computed directly. For simplicity, the grid points are defined to be uniform in the x , y , and z directions, with a grid size of d_g . The following description is of the four-step process involved in the PFFT technique to evaluate

matrix–vector products for pressure. Matrix–vector products for displacement can be evaluated similarly by separating the displacement into its three components and evaluating each component individually using the same PFFT procedure as for pressure, but with the Green’s functions for displacement.

1. Projection

As shown in Fig. 2(b), equivalent sources are projected onto the point sources placed at the vertices of the cells containing these equivalent sources. Consequently, an $N_x \times N_y \times N_z$ array of grid-point sources is used to replace the equivalent sources in all the cells (here, N_x , N_y , and N_z are the numbers of grid points in the x , y , and z directions, respectively, with $N_x N_y N_z = N_g$). One can obtain that

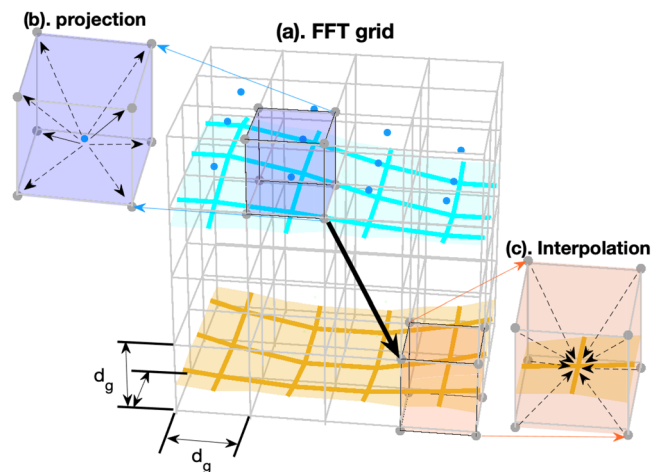


FIG. 2. (Color online) (a) FFT grid (gray dots) containing both the equivalent sources (orange dots) above the sea surface and their corresponding boundaries (cyan and khaki surfaces). (b) Projection of equivalent sources onto the FFT grid (shown in the blue cube) for evaluating the distant grid-to-grid interaction denoted by the bold arrow. (c) Interpolation of the field from the FFT grid to the nodes at the boundary (shown in the red cube).

$$\begin{aligned}
 &G(x, y, z; x_n^{eq}, y_n^{eq}, z_n^{eq} | k) \\
 &= \sum_{h,i,j} W_{h,i,j}(x_n^{eq}, y_n^{eq}, z_n^{eq}) G(x, y, z; x_h^g, y_i^g, z_j^g | k), \\
 &h = 1, 2, \dots, N_x, \quad i = 1, 2, \dots, N_y, \quad j = 1, 2, \dots, N_z,
 \end{aligned} \tag{5}$$

where the superscripts *eq* and *g* specify the coordinates of the equivalent sources and the grid points, respectively, and the triplet *h, i, j* and the subscript *n* specify the grid points in three dimensions and the *n*th equivalent source, respectively. Here, $W_{h,i,j}(x_n^{eq}, y_n^{eq}, z_n^{eq})$ is the spatial interpolation function for the coordinates (x_h^g, y_i^g, z_j^g) of the vertex of the cell that contains the equivalent source placed at $(x_n^{eq}, y_n^{eq}, z_n^{eq})$. Quadratic interpolation functions are used in this paper, and the construction of the spatial interpolation function follows the method presented by Yan and Liu (2011). Now, consider *N* equivalent sources with their source strengths $s_n(x_n^{eq}, y_n^{eq}, z_n^{eq})$:

$$\begin{aligned}
 &\sum_{n=1}^N s_n(x_n^{eq}, y_n^{eq}, z_n^{eq}) G(x, y, z; x_n^{eq}, y_n^{eq}, z_n^{eq} | k) \\
 &= \sum_{h,i,j} s_g(x_h^g, y_i^g, z_j^g) G(x, y, z; x_h^g, y_i^g, z_j^g | k).
 \end{aligned} \tag{6}$$

where $s_g(x_h^g, y_i^g, z_j^g) = \sum_{n=1}^N s_n(x_n^{eq}, y_n^{eq}, z_n^{eq}) W_{h,i,j}(x_n^{eq}, y_n^{eq}, z_n^{eq})$ is the total strength of the grid point source at (x_h^g, y_i^g, z_j^g) .

2. Convolution

As shown by the bold arrow in Fig. 2(a), once the equivalent sources have been projected onto the 3D array of grid points, the pressures on the grids due to the point sources on these grids can be evaluated by a 3D convolution (Phillips and White, 1997):

$$\begin{aligned}
 p(x_{h'}^g, y_{i'}^g, z_{j'}^g) &= \sum_{h,i,j} G(h' - h, i' - i, j' - j) s_g(h, i, j) \\
 &= \sum_{h,i,j} G(x_{|h'-h|}^g, y_{|i'-i|}^g, z_{|j'-j|}^g; x_0^g, y_0^g, z_0^g | k) \\
 &\quad \times s_g(x_h^g, y_i^g, z_j^g).
 \end{aligned} \tag{7}$$

For rapid evaluation of the 3D convolution, the 3D FFTs of the kernel array $G(h' - h, i' - i, j' - j)$ and the strength array $s_g(h, i, j)$ are first performed, followed by the inverse FFT of $\text{FFT}[G(h' - h, i' - i, j' - j)] \bullet \text{FFT}[s_g(h, i, j)]$, where \bullet denotes array multiplication.

3. Interpolation

After calculation of the pressure at the entry FFT grid points $p(x_{h'}^g, y_{i'}^g, z_{j'}^g)$ by the convolution, the pressures at arbitrary positions $p(x, y, z)$ within the grids can be evaluated by interpolating the fields from the grids to the desired field point using $W_{h',i',j'}(x, y, z)$, as shown in Fig. 2(c):

$$p(x, y, z) = \sum_{h',i',j'} W_{h',i',j'}(x, y, z) p(x_{h'}^g, y_{i'}^g, z_{j'}^g | k). \tag{8}$$

4. Precorrection

The projection of $G(\mathbf{r}(x, y, z); \mathbf{r}(x_n^{eq}, y_n^{eq}, z_n^{eq}) | k)$ becomes inaccurate when $|\mathbf{r} - \mathbf{r}_n^{eq}|/d_g < O(1)$. Therefore, for a very small source–receiver distance, the contribution due to exact near-field interaction should be directly added to Eq. (8), whereas that due to the influence determined by the 3D convolution should be subtracted from Eq. (8). In this paper, the near-field is defined by $|\mathbf{r} - \mathbf{r}_n^{eq}| < 3d_g$ such that precorrection is performed for receivers located in three cubes neighboring the equivalent sources. This means that when solving the linear system, only the submatrices $\mathbf{G}^{u,sp}(\mathbf{r}_b; \mathbf{r}_{(2i-1,2i)} | k)$ and $\mathbf{G}^{sp}(\mathbf{r}_a; \mathbf{r}_{(0)} | k)$ require precorrection.

C. Optimized scheme of FFT grids

A global FFT grid shown on the left in Fig. 3 is typically used to perform the PFFT procedure, covering all boundaries and the corresponding equivalent sources. Each additional layer treated in the simulation requires two additional sets of equivalent sources, and all steps involved in the PFFT are performed throughout the global FFT grid for each set of equivalent sources. Therefore, as the number of layers treated increases, the computational cost will increase proportionally. Real sound speed profiles (SSPs) are depth-dependent and need to be represented by a combination of layers within which the sound speed is piece-wise constant. In this case, the global FFT grid may be numerically expensive. Herein a scheme of FFT subgrids is used to reduce the computational cost in the scenarios of a stratified water column. The global FFT grid is broken into several FFT subgrids shown on the right in Fig. 3, each of which covers an individual layer and the equivalent sources near the upper and lower boundaries of the layer. Accordingly, each layer requires an individual PFFT procedure throughout the FFT subgrid that covers it. The computational efficiency is improved significantly by performing the PFFT procedure only throughout the FFT subgrid, rather than the global grid for each set of equivalent sources. Details of the comparison between the same case using the global FFT grid and the FFT subgrid is given in the following simulations.

III. NUMERICAL RESULTS

This section presents the results of numerical simulations. To benchmark the proposed PFFT-accelerated ESM (PFFT-ESM), propagation in shallow water with a Gaussian canyon was considered, and to show the PFFT-ESM’s capability for taking a sound speed profile into account, propagation in refractive water with the canyon was considered. To implement the PFFT-ESM, the sea surface and seabed were discretized uniformly in both the *x* and *y* directions with a $\lambda/6$ element size of the two adjacent nodes at the boundaries (d_e). The equivalent sources were then offset from their corresponding boundaries by a stand-off distance d_s equal to d_e . Such a stand-off distance provides a good compromise between computational accuracy and the diagonal dominance of the transfer matrix. For the PFFT parameters, the grid size d_g was set to be d_e , and the scale of the grid used

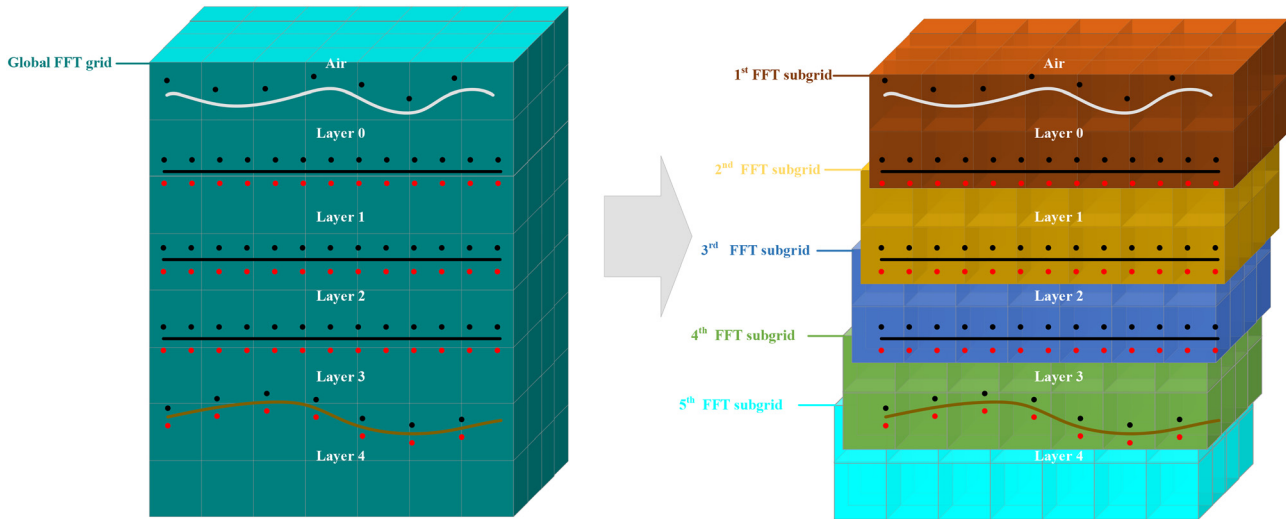


FIG. 3. (Color online) An example of the FFT subgrid scheme in a five-layered scenario with the global FFT grid shown on the left.

was as given below for each simulation. A Jacobian preconditioner was selected to accelerate the convergence rate of the iterative GMRM solver since submatrices in $[A]$ are diagonally dominant when $d_s = d_e$ is set. The GMRM halted iterations when the desired tolerance converged to 10^{-5} . All the simulations were implemented using MATLAB software (Matlab, Natick, MA) installed on a computer with an Intel Core i9–10900K CPU and 64 GB RAM (Intel, Santa Clara, CA).

A. Propagation over a multi-layered seabed

The proposed model was benchmarked by comparison with the longitudinal invariant finite element (LIFE) model (Isakson *et al.*, 2014) in the scenario of sound propagation over a Gaussian canyon. As shown in Fig. 4, the upper and lower layers of the sediment are described by $z_{b1}(x) = -100 - 400 \exp(-x^2/600^2)$ and $z_{b2}(x) = -200 - 400 \exp(-x^2/600^2)$ respectively, with the source placed at $(0 \text{ m}, 0 \text{ m}, -40 \text{ m})$. The source frequency was 20 Hz. A two-layered fluid seabed was assumed here, composed of a homogeneous sediment layer overlaying a homogeneous half-space (basement). The density, sound speed, and attenuation of the sediment were 2000 kg/m^3 , 1800 m/s , and $0.1 \text{ dB}/\lambda$ (where λ is the acoustic wavelength), respectively, and those of the basement were 2500 kg/m^3 , 3000 m/s , and $0.5 \text{ dB}/\lambda$, respectively. The computational domain size spans $4 \text{ km} \times 11 \text{ km} \times 637.5 \text{ m}$, with $N_g = 1.575 \times 10^7$ FFT grid points and $5N = 1.408 \times 10^6$ equivalent sources. It should be noted that a direct ESM solver requires at least 14770.5 GB RAM and $O(10^{12-18})$ operations, which is impractical. However, by incorporating PFFT, the proposed model can be run with a 64 GB RAM computer, and for the present problem, it took about 19.5 h to solve the linear system.

First, comparisons between the LIFE model and the proposed model are presented. Excellent agreements with the LIFE model can be seen in Figs. 5(a) and 5(b), where the transmission losses (TLs) are plotted in the $y = 0 \text{ m}$ and

the $x = 100 \text{ m}$ planes, respectively, with a receiver depth of 40 m, thus validating the proposed model. Figure 6(a) further displays the TL in the x – y plane at the same receiver depth, exhibiting apparent focusing patterns along the canyon axis due to the horizontal refraction. Besides, strong mode coupling effects (mode cutoff) occur as the sound wave propagates across the canyon, resulting in large across-canyon TL. The above results demonstrate the effectiveness of the proposed model in accurately modeling 3D underwater sound propagation including both the horizontal refraction and mode coupling effects.

Next, the applicability of the proposed model to calculate scattering from rough sea surfaces is demonstrated by modeling

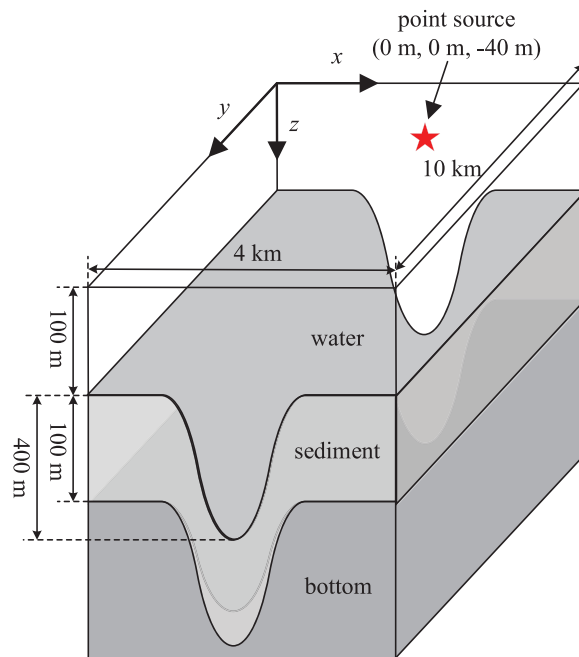


FIG. 4. (Color online) Scheme of the Gaussian canyon treated in the simulation.

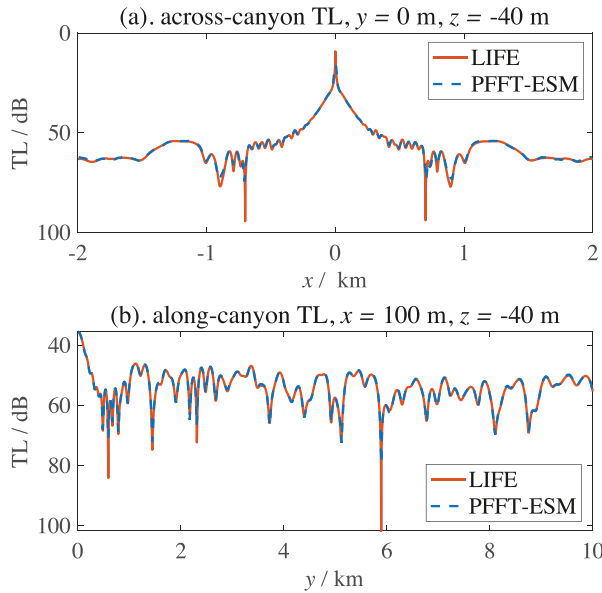


FIG. 5. (Color online) Comparisons of transmission losses with the LIFE model (red solid line) in: (a) the $y=0\text{ m}$ and (b) the $x=100\text{ m}$ planes respectively, with a receiver depth of -40 m at 20 Hz .

propagation in shallow water with the Gaussian canyon and corrugated surface waves. In this case, the corrugated surface waves oriented perpendicular and parallel, to the canyon axis were considered ($\theta = 90^\circ$ and $\theta = 0^\circ$ respectively where θ is the angle between the wave direction and the canyon axis), parameterized by $z_a(x, y) = -15 \cos(2\pi x/500)$ and $z_a(x, y) = -15 \cos(2\pi y/500)$, respectively. Figures 6(b) and 6(c) plots the corresponding TL in the $z = -40\text{ m}$ plane. By comparing the subplots in Fig. 6, it can be found that greater TLs are associated with the presence of the corrugated surface waves. This can be interpreted as indicating that energy transfer from lower modes to higher modes promotes more leakage of

energy in the seabed, associated with scattering from the corrugated surface wave. By further comparing Figs. 6(b) and 6(c), the case of $\theta = 90^\circ$ exhibits greater across-canyon TLs than the case of $\theta = 0^\circ$ does, with broader focusing patterns observed along the canyon axis. This is because the across-canyon corrugated surface wave mainly scatters sound waves propagating across the canyon but tends to channel sound waves along the canyon axis. On the contrary, scattering from the along-canyon corrugated surface wave mainly results in the energy decay along the canyon axis.

Then, Figs. 7 and 8 plot the across-canyon TL and the along-canyon TL in the $y = 0\text{ m}$ and the $x = 0$ planes, respectively, with the two wave orientations. For comparison purposes, the flat sea surface scenario is also given. In the across-canyon plane, more leakage of energy in the seabed can be seen in the presence of corrugated surface waves, coinciding with the above analysis. Compared with the case of $\theta = 0^\circ$, the case of $\theta = 90^\circ$ exhibits slightly stronger energy decays in the water column but smaller TLs in the sediment layer with the interference pattern indicating that at least two sediment modes are supported. In the along-canyon plane, scattering from corrugated surface waves induces more significant energy decay for longer distances, coinciding with the results shown in Fig. 6. Besides, The case of $\theta = 0^\circ$ exhibits apparent scattering features mainly ascribed to the in-plane scattering from the along-canyon corrugated surface wave, while the scattering effect in the case of $\theta = 90^\circ$ is ascribed to the out-of-plane scattering from the across-canyon corrugated surface wave.

B. Propagation in refractive water

Due to changes in temperatures and salinities in the water column, depth-dependent SSP strongly influence sound propagation in shallow water. BIE-based methods can

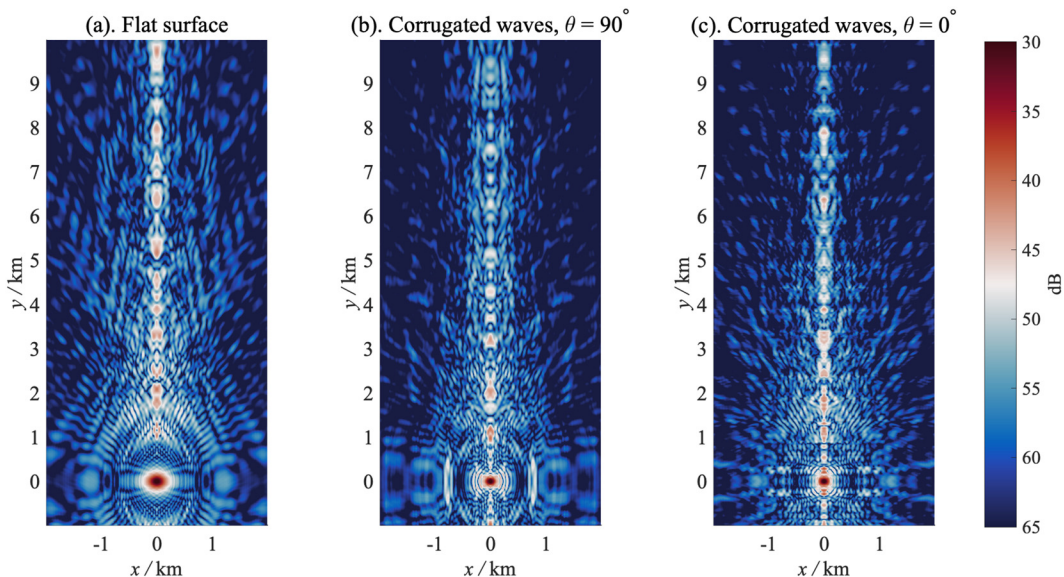


FIG. 6. (Color online) Transmission loss in shallow water over the Gaussian canyon with a receiver depth of $z = -40\text{ m}$. Here, (a), (b), and (c) displays scenarios of flat and corrugated surface waves, the latter oriented parallel and perpendicular to the canyon axis, respectively.

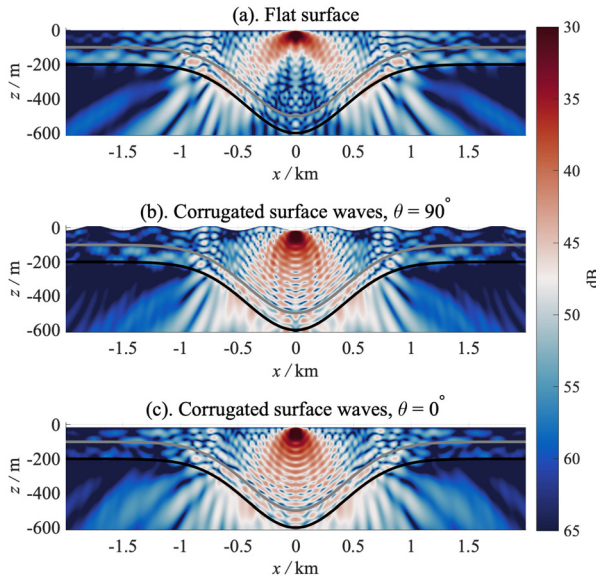


FIG. 7. (Color online) Transmission loss in shallow water over the Gaussian canyon within the $y = 0$ m, with subplots (a), (b), and (c) displaying scenarios of flat and corrugated surfaces, the latter oriented parallel and perpendicular to the canyon axis, respectively.

handle an inhomogeneous SSP by replacing the homogeneous Green's function with the inhomogeneous one (He *et al.*, 2021; Choo *et al.*, 2017). However, the accelerated algorithm assumes a homogeneous background (Cho and Cai, 2012), disabling the inhomogeneous Green's functions. Another way to introduce the SSP to the model is to divide the water column into layers where the SSP can be considered as a piece-wise constant approximately. Similar treatments to handle inhomogeneities in stratified media can be seen in the wavenumber integral approach (West *et al.*,

1991) and in the Helmholtz integral operator in 3D layered media (Cho and Cai, 2012). The following simulations demonstrate the PFFT-ESM's capability for propagation in refractive water with a two-layered summer profile. Such a simplified profile provides a good approximation to the actual situation in shallow water, where the sound speed varies significantly in the surface duct but changes steadily in deeper regions (Jensen *et al.*, 2011). Also, this section discusses the influences of the layer number and the sound speed gradients treated in the simulation.

When modeling propagation in refractive water, the source may be in an arbitrary layer. When the source is in the top layer, the right-hand side of the linear equation $\{b\}$ is given by Eq. (4). When the source is in layer i , $\{b\}$ is given by:

$$\{b\} = \left\{ \begin{array}{c} \vdots \\ \mathbf{p}_{inc}(\mathbf{r}_{b_i}) \\ \mathbf{u}_{inc}(\mathbf{r}_{b_i}) \\ -\mathbf{p}_{inc}(\mathbf{r}_{b_{i+1}}) \\ -\mathbf{u}_{inc}(\mathbf{r}_{b_{i+1}}) \\ \vdots \end{array} \right\}. \quad (9)$$

Here, the topography is described by $z_b(x) = -200 - 300 \exp(-x^2/600^2)$. The sound speed, density and attenuation of the seabed were 1500 kg/m^3 , 1700 m/s , and $0.5 \text{ dB}/\lambda$, respectively. The source was placed at $(0 \text{ m}, 0 \text{ m}, -175 \text{ m})$, with a source frequency of 20 Hz . The computational domain extends from $x = -1 \text{ km}$ to $x = 4 \text{ km}$, from $y = -2.5 \text{ km}$ to $y = 2.5 \text{ km}$ and from $z = -518.75 \text{ m}$ to $z = 18.75 \text{ m}$. Three SSPs treated in the simulations are shown in Fig. 9(a), with gradients $\Delta c = 60$, $\Delta c = 45$, and $\Delta c = 30 \text{ m/s}$ in the region of $-150 \text{ m} < z < 0 \text{ m}$. Four cases with different layers were considered. In the four-layered, three-layered, and two-layered cases, the region of $-150 \text{ m} < z < 0 \text{ m}$ was uniformly divided into three layers, two layers, and one layer along the depth axis, respectively, with the sound speed in each layer being the linear interpolation of the SSP (the mid-value of the exact sound speeds at the upper and lower boundaries of the layer). Below $z = -150 \text{ m}$, the sound speeds were set to be 1470 m/s , 1485 m/s and 1500 m/s for $\Delta c = 60$, $\Delta c = 45$, and $\Delta c = 30 \text{ m/s}$, respectively. For each Δc , the sound speed in the one-layered case was consistent with that below $z = -150 \text{ m}$ in other cases.

Figure 9(b) displays the TL along the $y = 0 \text{ m}$ axis with a receiver depth of -25 m for $\Delta c = 45 \text{ m/s}$, with the LIFE model's results shown in the solid black line as the reference. As the number of layers increases, the TL tends to converge to the reference. Also, root mean square errors (RMSEs) for different Δc are shown in Fig. 9(c), calculated using the pressure from $x = 0 \text{ km}$ to $x = 4 \text{ km}$. Overall, after decreasing rapidly, RMSEs start to converge when the layer thickness is about one wavelength (the thickness of layers dividing the region where the sound speed gradient occurs),

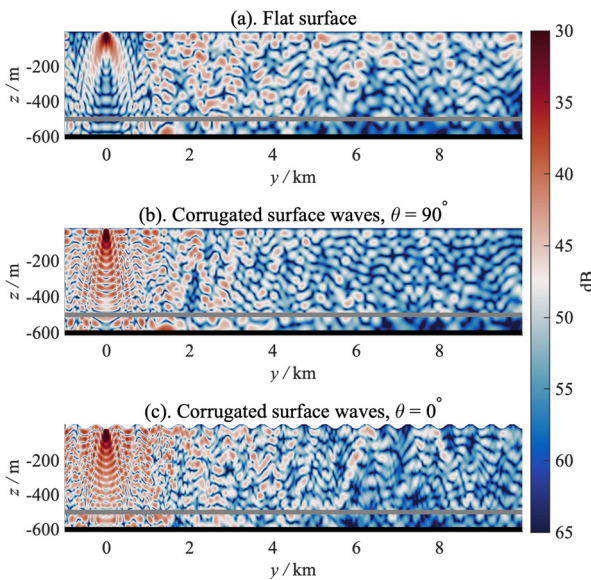


FIG. 8. (Color online) Transmission loss in shallow water over the Gaussian canyon within the $x = 0$ m, with subplots (a), (b), and (c) displaying scenarios of flat and corrugated surfaces, the latter oriented parallel and perpendicular to the canyon axis, respectively.

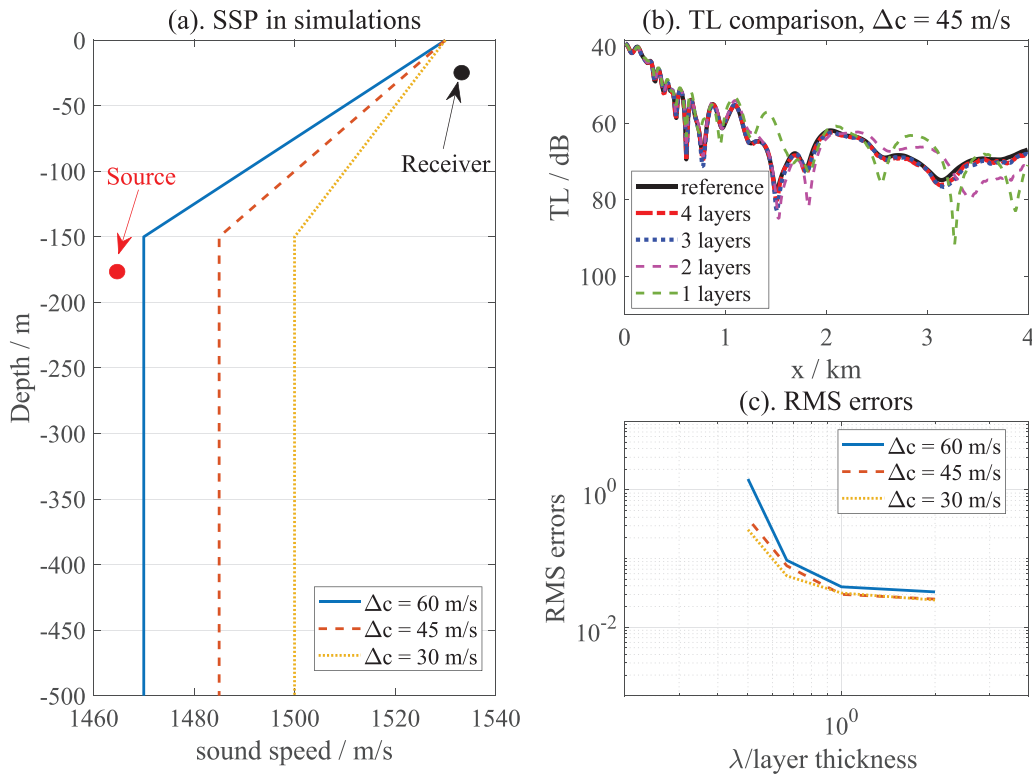


FIG. 9. (Color online) (a) Sound speed profiles treated in the simulations of propagation in refractive water, (b) comparisons between the transmission loss calculated by the PFFT-ESM with different layer schemes and that obtained by the LIFE model when $y = 0$ m and $z = -25$ m for $\Delta c = 45$ m/s, and (c) root mean square errors (RMSE) as a function of the ratio of the acoustic wavelength to layer thickness for different Δc .

which means that the layer thickness should be less than one wavelength to guarantee the accuracy in this case. Besides, decreases in RMSEs are associated with decreases in Δc , suggesting that larger Δc may require more layers to reduce the influence of weak discontinuities. A layer thickness of half wavelength or even quarter wavelength recommended by West *et al.* (1991) and Jensen *et al.* (2011), for instance, are suggested for SSP with larger gradients. The results demonstrate the capability of the PFFT-ESM for propagation in refractive water.

IV. DISCUSSIONS ON COMPUTATIONAL EFFICIENCIES

First, the feasibility of a fully 3D FE model for the present problem is discussed. The time and RAM required by the FE model depends on the degrees-of-freedom (DOF), which also is the expansion coefficients to be solved. For the Gaussian canyon with iso-velocity water, a trial of the fully 3D FE model was implemented. The physical domain was discretized using linear tetrahedrons with an element size of $1/6$ acoustic wavelength, composed of 2.842×10^8 elements

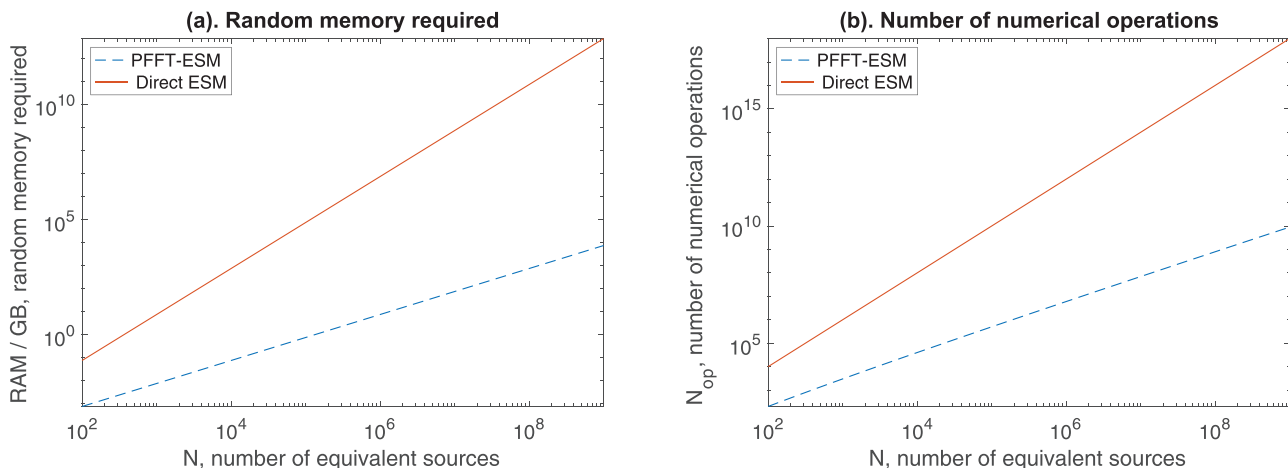


FIG. 10. (Color online) Random access memory and number of numerical operations required by the PFFT-ESM per iteration (blue dotted line) in comparison to those required by a direct ESM solver (red solid line).

TABLE I. Average time per iteration for the PFFT-ESM using the global FFT grid and the FFT subgrid.

	Iso-velocity water simulation		Refractive water simulation		
	Multi-layered seabed case (s)	Four-layered case (s)	Three-layered case (s)	Two-layered case (s)	One-layered case (s)
Global FFT grid	54	54	43	29	13
FFT subgrid	47	18	15	12	10

with a DOF number of 3.8385×10^8 . This number was significantly larger than the number of unknowns in the PFFT-ESM. Although existing commercial FE software optimizes the iterative solver for the linear system, such a large DOF requires tremendous computational resources, making the fully 3D FE model remain computationally challenging for the present problem to be run on a standard computer. The trial ended up with the software crashing at the step of matrix assembly due to insufficient RAM. Additional computational resources, such as supercomputers or multi-computer clusters, may be required to implement the fully 3D FE model. This is the reason why LIFE was alternatively used as the benchmark.

Then, RAM required and numerical operations involved in the PFFT-ESM per iteration are discussed by plotting those as a function of the number of equivalent sources in Fig. 10. For comparison purposes, the case of a direct ESM solver is also shown in Fig. 10. From Sec. II B, it is known that 3D convolution, the most numerically expensive operation step in the PFFT, costs $O(N_g \log N_g)$ operations. Generally, N_g is on the same order as N . For all simulations presented in this paper, double precision arrays are involved in the calculations, with each element of the arrays requiring 8 bytes RAM to be stored. Therefore, the PFFT-ESM requires $O(8N/1.048 \times 10^6)$ GB RAM to store the arrays and approximately costs $O(N \log N)$ operations to calculate each iteration. By contrast, the direct ESM needs $O(N^2)$ operations to calculate the iteration, taking up $O(8N^2/1.048 \times 10^6)$ GB RAM to store the corresponding arrays. When N is large, memory savings and significantly reduced operations are achieved by incorporating the PFFT with the ESM, enabling an efficient 3D numerical solution of the Helmholtz equation that modern PC platforms can solve. It should be noted that the distant source-receiver interaction is represented by a locally weighted grid-to-grid interaction that corresponds to the grids covering the source and the receiver, which means that projection and interpolation matrices are sparse. Therefore, the numerical cost is much smaller than that of the finite difference method or the FEM, which resorts to a similar grid throughout the physical domain.

Next, Table I shows the average time per iteration for the PFFT-ESM using the global FFT grid and the FFT subgrid in the same case. In the refractive simulation, the FFT subgrid scenario is about three times faster than the global grid scenario. Although the layer number quintuples from the one-layered case to the five-layered case, the average time per iteration only increases by 8 s using the FFT subgrid scheme. In the iso-velocity water simulation, the FFT

subgrid scheme only saves 13% computation time because the size of the subgrid covering each layer approaches that of the global grid. This demonstrates the computational efficiency improved by the FFT subgrid scheme, particularly when the water column needs to be represented by a combination of layering.

V. CONCLUSIONS

A 3D underwater acoustic propagation model based on the equivalent source method has been developed, enabling a direct numerical solution of the Helmholtz equation for large-scale propagation at a reasonable computational cost. The model expresses the solution of the Helmholtz equation in terms of a superposition of the fields generated by equivalent sources and iteratively solves the unknown coefficients of these equivalent sources using the generalized minimum residual method. By evaluating the matrix-vector product in each iteration using the pre-corrected fast Fourier transform technique, the computational cost can be reduced from $O(N^{2-3})$ to $O(N_g \log N_g)$ (where N and N_g are the numbers of equivalent sources and FFT grid points, respectively). An optimized FFT subgrid scheme has been proposed to improve the model's numerical efficiencies further, especially when multiple layers are required to divide the water column, e.g., the sound speed is treated as a piece-wise constant. The proposed model has been validated by comparison with the longitudinal invariant finite element model for propagation in shallow water with a Gaussian canyon. The versatility of the proposed model for showing rough scattering effects has been demonstrated by further presenting the Gaussian canyon simulations with corrugated surface waves. The results indicate that the along-canyon corrugated surface waves result in weaker focusing effects while the across-canyon corrugated surface waves induce more significant energy decays for acoustic waves propagating across the canyon.

ACKNOWLEDGMENTS

This work was supported by the National Natural Science Foundation of China under Grant No. 11674075. The authors warmly thank the two anonymous reviewers for excellent comments and suggestions, which helped improve this paper significantly.

Abawi, A. T., and Porter, M. B. (2007). "Propagation in an elastic wedge using the virtual source technique," *J. Acoust. Soc. Am.* **121**(3), 1374–1382.

- Bottero, A., Cristini, P., Komatitsch, D., and Asch, M. (2016). "An axisymmetric time-domain spectral-element method for full-wave simulations: Application to ocean acoustics," *J. Acoust. Soc. Am.* **140**(5), 3520–3530.
- Bottero, A., Cristini, P., Komatitsch, D., and Brissaud, Q. (2018). "Broadband transmission losses and time dispersion maps from time-domain numerical simulations in ocean acoustics," *J. Acoust. Soc. Am.* **144**(3), EL222–EL228.
- Cho, M. H., and Cai, W. (2012). "A parallel fast algorithm for computing the helmholtz integral operator in 3-d layered media," *J. Comput. Phys.* **231**(17), 5910–5925.
- Choo, Y., Song, H., and Seong, W. (2017). "Time-domain helmholtz-kirchhoff integral for surface scattering in a refractive medium," *J. Acoust. Soc. Am.* **141**(3), EL267–EL273.
- Collins, M. D., and Evans, R. B. (1992). "A two-way parabolic equation for acoustic backscattering in the ocean," *J. Acoust. Soc. Am.* **91**(3), 1357–1368.
- Cristini, P., and Komatitsch, D. (2012). "Some illustrative examples of the use of a spectral-element method in ocean acoustics," *J. Acoust. Soc. Am.* **131**(3), EL229–EL235.
- Godinho, L., Tadeu, A., and Branco, F. (2001). "3d acoustic scattering from an irregular fluid waveguide via the bem," *Eng. Anal. Bound. Elem.* **25**(6), 443–453.
- He, T., Humphrey, V. F., Mo, S., and Fang, E. (2020). "Three-dimensional sound scattering from transversely symmetric surface waves in deep and shallow water using the equivalent source method," *J. Acoust. Soc. Am.* **148**(1), 73–84.
- He, T., Mo, S., Guo, W., and Fang, E. (2021). "Modeling propagation in shallow water with the range-dependent sea surfaces and fluid seabeds using the equivalent source method," *J. Acoust. Soc. Am.* **149**(2), 997–1011.
- Isakson, M. J., and Chotiros, N. P. (2011). "Finite element modeling of reverberation and transmission loss in shallow water waveguides with rough boundaries," *J. Acoust. Soc. Am.* **129**(3), 1273–1279.
- Isakson, M. J., Goldsberry, B., and Chotiros, N. P. (2014). "A three-dimensional, longitudinally-invariant finite element model for acoustic propagation in shallow water waveguides," *J. Acoust. Soc. Am.* **136**(3), EL206–EL211.
- Jensen, F. B., Kuperman, W. A., Porter, M. B., and Schmidt, H. (2011). *Computational Ocean Acoustics* (Springer Science & Business Media, New York), pp. 3, 4, 140, 226, 466.
- Koopmann, G. H., Song, L., and Fahline, J. B. (1989). "A method for computing acoustic fields based on the principle of wave superposition," *J. Acoust. Soc. Am.* **86**(6), 2433–2438.
- Li, C., Campbell, B. K., Liu, Y., and Yue, D. K. (2019). "A fast multi-layer boundary element method for direct numerical simulation of sound propagation in shallow water environments," *J. Comput. Phys.* **392**, 694–712.
- Lingevitch, J. F., Collins, M. D., Mills, M. J., and Evans, R. B. (2002). "A two-way parabolic equation that accounts for multiple scattering," *J. Acoust. Soc. Am.* **112**(2), 476–480.
- Pereira, A., Tadeu, A., Godinho, L., and Santiago, J. (2010). "2.5 d bem modeling of underwater sound scattering in the presence of a slippage interface separating two flat layered regions," *Wave Motion* **47**(8), 676–692.
- Phillips, J. R., and White, J. K. (1997). "A precorrected-fft method for electrostatic analysis of complicated 3-d structures," *IEEE Trans. Comput.-Aided Design Integr. Circuits Syst.* **16**(10), 1059–1072.
- Porter, M. B. (2019). "Beam tracing for two- and three-dimensional problems in ocean acoustics," *J. Acoust. Soc. Am.* **146**(3), 2016–2029.
- Siderius, M., and Porter, M. B. (2008). "Modeling broadband ocean acoustic transmissions with time-varying sea surfaces," *J. Acoust. Soc. Am.* **124**(1), 137–150.
- Sturm, F. (2016). "Leading-order cross term correction of three-dimensional parabolic equation models," *J. Acoust. Soc. Am.* **139**(1), 263–270.
- West, M., Sack, R., and Walkden, F. (1991). "The fast field program (ffp). a second tutorial: Application to long range sound propagation in the atmosphere," *Appl. Acoust.* **33**(3), 199–228.
- Xie, Z., Matzen, R., Cristini, P., Komatitsch, D., and Martin, R. (2016). "A perfectly matched layer for fluid-solid problems: Application to ocean-acoustics simulations with solid ocean bottoms," *J. Acoust. Soc. Am.* **140**(1), 165–175.
- Yan, H., and Liu, Y. (2011). "An efficient high-order boundary element method for nonlinear wave-wave and wave-body interactions," *J. Comput. Phys.* **230**(2), 402–424.